A Satellite Analysis of Deep Convection, Upper-Tropospheric Humidity, and the Greenhouse Effect

BRIAN J. SODEN* AND RONG FU†

Atmospheric and Oceanic Sciences Program, Princeton University, Princeton, New Jersey

(Manuscript received 28 October 1994, in final form 22 March 1995)

ABSTRACT

This paper combines satellite measurements of the upwelling 6.7-μm radiance from TOVS with cloud-property information from ISCCP and outgoing longwave radiative fluxes from ERBE to analyze the climatological interactions between deep convection, upper-tropospheric humidity, and atmospheric greenhouse trapping. The satellite instruments provide unmatched spatial and temporal coverage, enabling detailed examination of regional, seasonal, and interannual variations between these quantities. The present analysis demonstrates that enhanced tropical convection is associated with increased upper-tropospheric relative humidity. The positive relationship between deep convection and upper-tropospheric humidity is observed for both regional and temporal variations, and is also demonstrated to occur over a wide range of space and time scales. Analysis of ERBE outgoing longwave radiation measurements indicates that regions or periods of increased upper-tropospheric moisture are strongly correlated with an enhanced greenhouse trapping, although the effects of lower-tropospheric moisture and temperature lapse rate are also observed to be important. The combined results for the Tropics provide a picture consistent with a positive interrelationship between deep convection, upper-tropospheric humidity, and the greenhouse effect. In extratropical regions, temporal variations in upper-tropospheric humidity exhibit little relationship to variations in deep convection, suggesting the importance of other dynamical processes in determining changes in upper-tropospheric moisture for this region. Comparison of the observed relationships between convection, upper-tropospheric moisture, and greenhouse trapping with climate model simulations indicates that the Geophysical Fluid Dynamics Laboratory (GFDL) GCM is qualitatively successful in capturing the observed relationship between these quantities. This evidence supports the ability of the GFDL GCM to predict upper-tropospheric water vapor feedback, despite the model's relatively simplified treatment of moist convective processes.

1. Introduction

Water vapor is the principal greenhouse gas and plays a pivotal role in regulating the earth's climate and its sensitivity to increasing greenhouse gases. Present estimates suggest that water vapor feedback increases climate sensitivity by a factor of roughly 1.6 (IPCC 1990). However, the reliability of such estimates has been called into question due to uncertainties in predicting feedbacks involving upper-tropospheric water vapor. Specifically, Lindzen (1990) suggests that increased convection in a warmer climate would dry the upper troposphere through enhanced subsidence in regions surrounding the convective towers. Moreover, due to their simplified treatment of moist convective processes, it has been speculated that general circulation models are inadequate for representing this feedback and, consequently, that present GCMs may inaccurately estimate the role of upper-tropospheric water vapor feedback in amplifying global warming.

A scarcity of reliable observations of upper-tropospheric water vapor has hindered direct verification of this hypothesis. Conventional observations from radiosondes provide only limited spatial coverage and are of questionable reliability in the upper troposphere (Elliot and Gaffen 1991). Consequently, a clear understanding of how changes in deep convection modify the moisture content of the upper troposphere has been illusive. Fortunately, recent studies have described summary datasets of clear-sky water vapor radiances from the 6.7-μm channel onboard geostationary (Soden and Bretherton 1993; Schmetz and Turpeinen 1988) and polar orbiting (Wu et al. 1993) satellites, which can yield valuable insight into this issue. These measurements provide information regarding the vertically averaged water vapor content of the upper troposphere (roughly 200–500 mb).

Although archived observations of the 6.7-μm radiances have been available since the late 1970s, this

* Current affiliation: NOAA/Geophysical Fluid Dynamics Laboratory.

† Current affiliation: Institute of Atmospheric Physics, University of Arizona.

Corresponding author address: Dr. Brian J. Soden, NOAA/Geophysical Fluid Dynamics Laboratory, Princeton University, Forrestal Campus, P.O. Box 308, Princeton, NJ 08542.
E-mail: bjs@gfdl.gov

information has been largely unutilized for climate studies. One reason for the lack of attention is due to the difficulty in interpreting the observed radiances in terms of a more familiar water vapor quantity. Soden and Bretherton (1993) addressed this issue by developing an interpretation tool based upon a simplified theoretical model of radiative transfer at 6.7 μm. This tool provides a convenient means of interpreting the observed water vapor radiances in terms of an upper-tropospheric humidity index (UTH). A brief description of this interpretation tool is provided in section 2b.

Recent studies by Rind et al. (1991) and Inamdar and Ramanathan (1994) examined the influence of deep convection on the distribution of upper-tropospheric moisture. Rind et al. (1991) compared Stratospheric Aerosol and Gas Experiment (SAGE II) measurements of upper-tropospheric moisture between ascending and descending regions of the Hadley and Walker circulation. They found greater moisture in the ascending regions relative to the descending regions, consistent with the conventional picture of deep convection serving to moisten the upper troposphere. Inamdar and Ramanathan (1994) categorized radiosonde profiles of water vapor into convective and nonconvective categories based upon the corresponding SST. They also observed greater moisture in regions of highest SST and demonstrated the importance of this on the surface and the top-of-atmosphere radiative energy budget. While these studies contrasted moisture profiles between convective and nonconvective areas, neither of them explicitly examined the relationship between convective activity and upper-tropospheric moisture. They basically compared differences between regions of large-scale ascent and descent. Variations in moisture between these regions are generally closely associated with each other in a compensating fashion. Thus, while convection may moisten the upper troposphere locally, it is not obvious how the net moisture budget will change when averaged over larger domains, which include regions of both large-scale ascent and descent. Consequently, it is important to examine the sensitivity of the relationship between convection and upper-tropospheric moisture to the spatial scale of the analysis.

This investigation combines satellite observations of deep convection, upper-tropospheric water vapor, and the clear-sky outgoing longwave radiation (OLR) to examine how convective activity influences the distribution of upper-tropospheric moisture and its resulting impact upon the OLR. Unique features of this study include: 1) the use of TOVS 6.7-μm radiances to describe the global distribution of upper-tropospheric water vapor; 2) the use of satellite measurements of deep convective clouds to directly relate convective activity to upper-tropospheric moisture, rather than inferring this relationship from seasonal changes in the large-scale circulation or a dependence upon SST; and 3) the greatly improved spatial and temporal coverage of the TOVS upper-tropospheric moisture measurements, unmatched by either SAGE or radiosonde datasets, which enable detailed examination of regional and temporal interactions between convection, upper-tropospheric moisture, and greenhouse trapping over a wide range of space and time scales.

Specifically, this paper addresses the following questions: 1) How are spatial/temporal variations in convection, upper-tropospheric moisture, and the outgoing longwave radiation related to one another?; 2) How do these local relationships depend upon the spatial scale of the analysis?; 3) How are the interannual variations between deep convection, upper-tropospheric moisture, and outgoing longwave radiation coupled on the large scale?; 4) To what extent can GCMs reproduce the observed relationships?

The rest of this paper is organized as follows. Section 2 describes the satellite data sources of deep convection, upper-tropospheric humidity, and outgoing longwave radiation and their application in the present study. Section 3 examines the relationships between these quantities inferred from spatial variations at both local and regional scales. Sections 4 and 5 investigate the temporal interactions on seasonal and interannual timescales. Section 6 compares the observational results with simulations from the GFDL GCM and section 7 discusses the conclusions of this study.

2. Datasets and methodology

a. Deep convection

This study employs observations from the International Satellite Cloud Climatology Project (ISCCP) to provide estimates of convective activity using high, optically thick cloud cover as a proxy for deep convection. Deep convective cloud is diagnosed by using the ISCCP C2 monthly mean cloud dataset. This dataset provides estimates of cloud optical thickness and cloud-top pressure determined from radiative transfer calculations using ISCCP visible (0.6 μm) and infrared (11.0 μm) radiances and vertical profiles of temperature, humidity, and trace gases provided by other remote sensing data or climatology (Rossow and Schiffer 1991). Deep convective clouds are defined as those cloudy pixels for which the optical thickness is greater than 22.4 and the cloud-top pressure is lower than 440 mb. The optical thickness threshold is approximately equivalent to an albedo of 0.7, suggested by both theoretical calculation (e.g., Liou 1976) and sensitivity analysis of the ISCCP radiances (Fu et al. 1990). The frequency of deep convection (FDC) represents the number of pixels classified as deep convective clouds (size of 5–8 km sampled to approximately 30-km spacing) in a 2.5° × 2.5° latitude–longitude grid cell, which is at a scale comparable to a deep convective cluster. The FDC can also be interpreted as an index of fractional amount of deep convective clouds if it is

divided by the number of total pixels in the same 2.5° × 2.5° grid cell (~64). Although the precise value of the FDC index may be limited by uncertainties in ISCCP retrieval method, this study emphasizes the patterns of spatial and temporal variation in FDC, which are robust features of the ISCCP dataset and are consistent with other satellite estimates of convective activity (e.g., Waliser et al. 1993). This is particularly true for the Tropics, where deep convection is the primary mechanism for generating thick high clouds. Furthermore, as demonstrated by Lau and Crane (1995), deep convective clouds detected by ISCCP are also consistent with the dynamic fields derived from operational analyses even at the synoptical scale. However, greater uncertainty in the FDC index may occur over midlatitudes where multilayer clouds (e.g., nimbostratus along fronts that may or may not have embedded convection) could cause some overestimation of the FDC. Consequently, the results for extratropical regions should be interpreted with some caution. The global distribution of monthly mean FDC is reported for eight UTC times as well as the daily mean. We use the daily mean global distribution of monthly frequency of deep convective clouds.

b. *Upper-tropospheric humidity*

To describe the regional and temporal variations of upper-tropospheric moisture, clear-sky measurements in the 6.7-μm channel are obtained from the TIROS Operational Vertical Sounder (TOVS) for the period of 1983–90. The TOVS 6.7-μm radiance measurements are obtained from NOAA operational polar-orbiting satellites. The National Environmental Satellite Data and Information Service (NESDIS) processes the data, yielding clear-sky, limb-corrected radiances, which are horizontally averaged onto a roughly 200 km × 100 km grid. The limb correction converts radiances observed at varying zenith angles to equivalent zenith-viewed radiances. Additional details regarding the TOVS instrument and NESDIS processing are provided by Wu et al. (1993) and Kidwell (1991). The 6.7-μm channel is located near the center of a strong water vapor absorption band, and under clear-sky conditions is sensitive primarily to the relative humidity averaged over a broad layer centered in the upper troposphere (Soden and Bretherton 1993). The position of this layer shifts somewhat depending upon the moisture and temperature of the atmosphere, being slightly higher for warm/moist profiles and slightly lower for cold/dry profiles. Figure 1 illustrates the approximate sensitivity of the 6.7-μm brightness temperature ($T_{6.7}$) to changes in relative humidity at various pressure for a typical tropical and midlatitude profile viewed at zenith.

To facilitate the interpretation of $T_{6.7}$ in terms of a more familiar water vapor quantity, Soden and Bretherton (1993) developed an interpretation tool based upon a simplified theoretical model of radiative transfer. Using the Goody random band model and assuming strongly absorbing, pressure-broadened lines, Soden and Bretherton (1993) demonstrated that, to a good approximation (±1 K), $T_{6.7}$ is proportional to the natural logarithm of a parameter "UTH," which corresponds to the relative humidity vertically averaged over a range of pressures in the upper troposphere (roughly 200–500 mb; see Fig. 1). Based on this model of radiative transfer, a theoretical relationship between the $T_{6.7}$ and the vertically averaged relative humidity (UTH) was obtained:

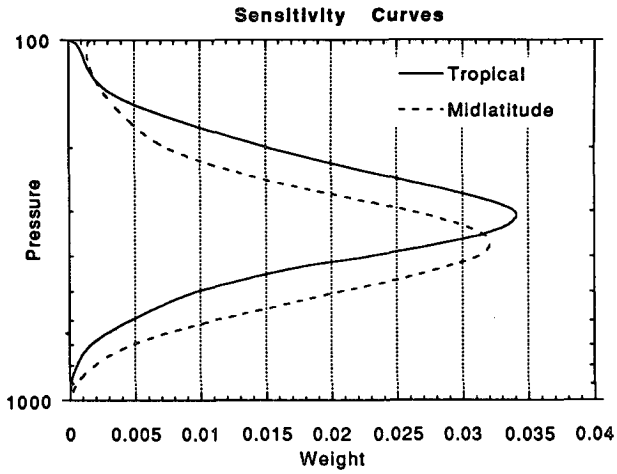

FIG. 1. A profile of the sensitivity of $T_{6.7}$ to variations in relative humidity in thin layers of atmosphere, equally spaced in the logarithm of pressure ($\Delta \ln(p) = dp/p = 0.04$), for a typical tropical (solid line) and midlatitude (dashed line) profile. The sum of weights is equal to unity.

$$\log_e\left(\frac{\mathrm{UTH}\,p'}{\cos\theta}\right) = a + bT_{6.7}, \qquad (1)$$

where θ is the satellite zenith angle, $p' = p_0/p_*$ is a normalized pressure variable composed of $p_* = 300$ mb, a fixed reference pressure for the water vapor absorption line width, and p_0, a variable base pressure at which the temperature of a climatological profile is 240 K (Soden and Bretherton 1993). The base pressure p_0 is determined monthly for each 2.5° latitude belt using a zonally averaged temperature climatology from the European Centre for Medium-Range Weather Forecasts (ECMWF). Since all 6.7-μm radiances examined here have been adjusted to equivalent nadir-view ($\theta = 0$) radiances, $\cos\theta = 1$ in Eq. (1). In essence, UTH is simply a transformed brightness temperature that, to a good approximation (±8%), represents a measure of the relative humidity averaged over a broad layer in the upper troposphere (roughly 200–500 mb). The coefficients $a = 31.50$, $b = -0.1136\ \mathrm{K}^{-1}$ are determined by comparing synthetic $T_{6.7}$, calculated from representative profiles of temperature and moisture, with

the corresponding vertically averaged upper-tropospheric relative humidity obtained from the same profiles, and are in good agreement with the theoretically expected values (Soden and Bretherton 1993). The reader is referred to Soden and Bretherton (1993, 1995) for a detailed discussion and derivation of Eq. (1).

To verify the reliability of satellite observations of upper-tropospheric moisture, Soden et al. (1994) compared GOES (Geostationary Operational Environmental Satellite) UTH measurements with state-of-the-art observations from Raman lidar and Cross-chain Loran Atmospheric Sounding System (CLASS) instruments. The satellite observations exhibited very good agreement with both sets of independent measurements. Typical rms differences between the satellite and CLASS/lidar measurements were approximately 7% in terms of a vertically averaged upper-tropospheric relative humidity (i.e., UTH), with correlations greater than 0.9. The study by Soden et al. (1994) compared measurements from the GOES Visible and Infrared Spin Scan Radiometer (VISSR) Atmospheric Sounder (VAS), whereas the TOVS measurements are analyzed here. However, both instruments measure $T_{6.7}$ using nearly identical spectral response functions and have similar levels of instrumental noise (0.75–0.9 K). Hence, the comparison statistics cited above should be representative for TOVS measurements as well.

Since clouds strongly attenuate IR radiation, measurements of UTH are not available from overcast pixels. Specifically, NESDIS does not provide clear sky $T_{6.7}$ in conditions where the cloud cover for a 200 km by 100 km grid box exceeds 75%. Because pixels identified to be convective are by definition cloudy, comparisons between FDC and UTH cannot be made on a pixel by pixel basis. In this study, we examine variations between monthly mean FDC and UTH, and thus are focusing on the effects of deep convection in moistening the environment rather than on the effects locally within the convective tower. However, the lack of measurements from overcast pixels is expected to introduce a dry bias into the UTH climatology. The magnitude of this bias is not well known; however, preliminary analysis suggests that it is less than 5%–10% in terms of the relative humidity (Soden et al. 1994).

Recently, Bates and Wu (1995) have noted calibration differences between various TOVS instruments ranging from 0.1 to 0.4 K. As noted by Soden and Bretherton (1993), changes in the calibration of the 6.7-μm channel for one satellite would simply yield a constant offset and not affect the spatial or temporal variability of the UTH field, which is the subject of the present study. It is conceivable that changes in calibration of the 6.7-μm channel from one satellite to the next could introduce spurious temporal variations in the UTH field. However, Soden and Bretherton (1995) indicate that the dominant mode of interannual variation in UTH examined here is not sensitive to the changes in 6.7-μm calibration.

c. *Outgoing longwave radiation*

To explore how variations in deep convection and upper-tropospheric moisture affect the radiative energy budget, observations of the broadband outgoing longwave radiation at the top of the atmosphere are obtained from the Earth Radiation Budget Experiment (ERBE). ERBE measurements provide radiative fluxes for both a total and clear-sky atmosphere. This study uses clear-sky OLR measurements averaged onto monthly mean 2.5° × 2.5° grids for the period February 1985–January 1989.

Insight into the broadband radiative effect of water vapor can be obtained by examining the normalized clear-sky greenhouse effect g (Raval and Ramanathan 1989) defined as

$$g = \frac{\sigma T_s^4 - F_c}{\sigma T_s^4}, \tag{2}$$

where T_s is the surface temperature, F_c is the clear-sky OLR, and σ is the Stephan–Boltzman constant. Due to the uncertainty in surface temperatures over land (Wu and Chang 1991), determination of g is restricted to ocean surfaces. Previous studies (Raval and Ramanathan 1989; Stephens 1990) have shown a strong dependence of g upon SST reflecting the increase water vapor mass with temperature dictated by the Clausius–Clapeyron equation. Using thermodynamic arguments, Raval and Ramanathan (1989) demonstrated that g varies approximately linearly with SST. This results from the observation that g scales linearly with the natural log of the precipitable water and that the precipitable water scales exponentially with SST. This study is largely interested in how g is affected by dynamical processes (i.e., convection, subsidence) rather than thermodynamical processes (i.e., Clausius–Clapeyron relationship). In this regard, greater understanding of the dynamical characteristics of the greenhouse effect can be obtained by considering the observed departure of g from that expected based upon thermodynamic principles. In a manner similar to Stephens et al. (1993), we define a dynamical greenhouse parameter g^*:

$$g^* = \frac{g - \bar{g}}{\bar{g}}, \tag{3}$$

where $\bar{g}$ is determined by linear regression of g versus SST (Reynolds 1988) using a 4-year average of these quantities. The local departure of g from the climatological g–SST relation is a measure of the impact of dynamical processes on the greenhouse effect through the redistribution of atmospheric moisture (Stephens et al. 1993).

3. Regional correlation analysis

a. Deep convection and upper-tropospheric humidity

To illustrate the basic patterns of geographic variation of deep convection and upper-tropospheric humidity, maps of these quantities are presented in Fig. 2. The data displayed in these maps correspond to time averages over the period July 1983–June 1990. Both quantities exhibit notable geographic variations that are consistent with well-known patterns of the large-scale atmospheric circulation. In particular, the coarse geographic distribution of UTH displays a striking similarity to the patterns of deep convection, although some inconsistencies between the finer details of the patterns are apparent (e.g., over the equatorial Atlantic from 0°–60°W). Maxima in FDC and UTH occur in a well-defined band over the tropical oceans, delineating the ITCZ, with broader regions of maxima over the western Pacific warm pool and monsoonal regions of central Africa and northern Brazil. Typical values of FDC in these regions range from 8% to 12%, with the larger values occurring over Central America and

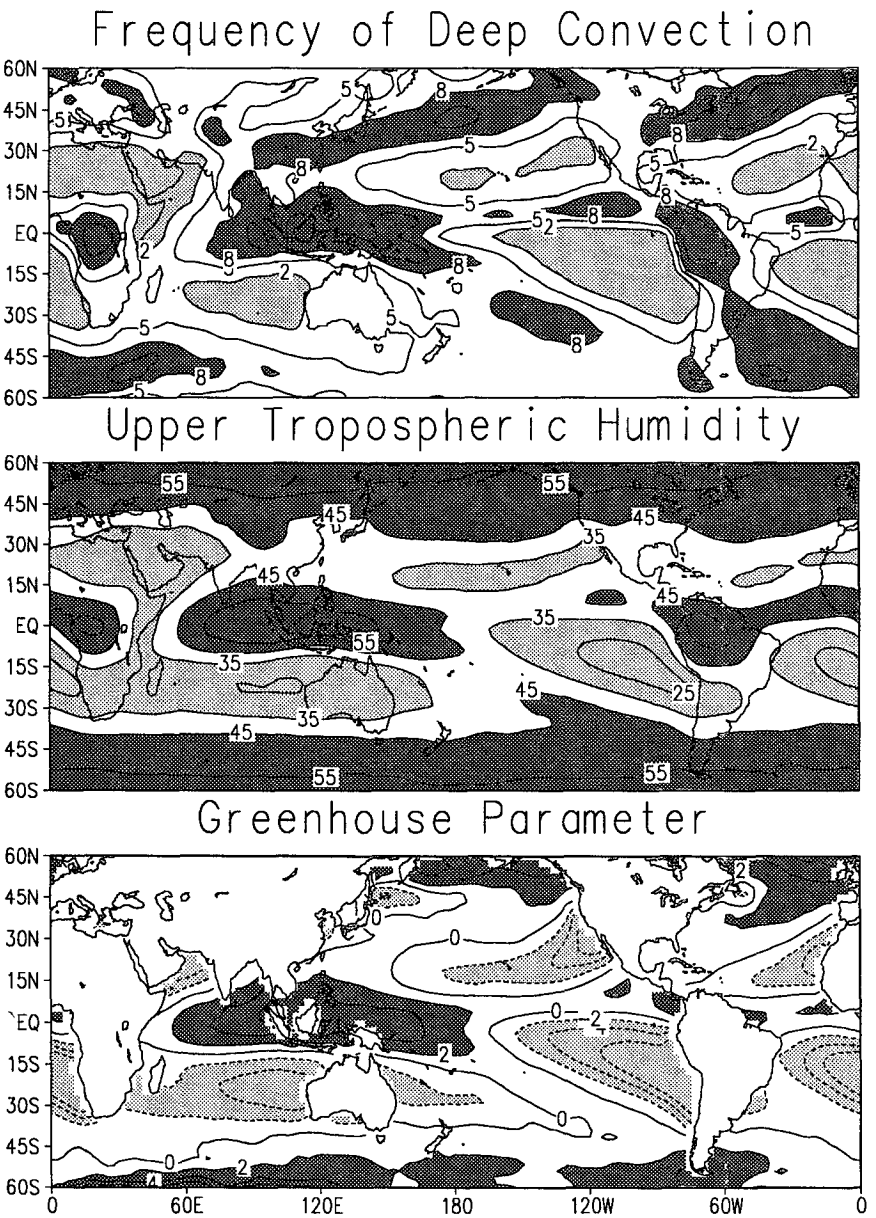

FIG. 2. Geographic maps of the annual average frequency of deep convection (top), upper-tropospheric humidity (middle), and dynamical greenhouse parameter g^* (bottom). Contour intervals are 3% (top), 10% (middle), and 2% (bottom).

the western Pacific. Maximum UTH range from roughly 40% along the ITCZ to nearly 60% in the western Pacific. Over the subtropics, both FDC and UTH exhibit broad bands of minima, indicating that where the deep convection is less frequent, the atmosphere is drier. The strong similarity between the distributions of deep convection and upper-tropospheric humidity, particularly within the 30°N–30°S tropical belt, suggests that *locally* (i.e., on the scale of a 2.5° × 2.5° grid box) deep convection serves to moisten the upper troposphere. Over the midlatitude oceans both FDC and UTH show regions of relative maxima; however, the similarity between the two fields is noticeably lower. Since temperature variations in the Tropics are small (Sun and Oort 1994; Oort 1983), the regional variations in specific humidity in the tropical upper troposphere closely match the variations in UTH.

To quantify the extent of the correlation between geographic variations of convection and upper-tropospheric moisture, Fig. 3a shows a scatter plot of FDC versus UTH. To focus on the relationship between tropical convection and UTH, the analysis is restricted to latitudes between 30°N and 30°S. Each data point corresponds to a 2.5° grid box for which the observations were averaged over the entire 7-year period July 1983–June 1990. The primary feature of this scatter plot is a distinct positive trend between FDC and UTH, indicating that regions with greater convective activity are associated with increased upper-tropospheric moisture. On average the UTH doubles from ~30% in regions with little convection (FDC < 2) to ~60% in regions of frequent convective activity (FDC > 12). The correlation (r = 0.82) is significant at the 99% level for a minimum of 6 degrees of freedom and indicates that regional variations in convective activity explain roughly 65% of the variability in UTH. This is consistent with the conventional view that deep convection serves to moisten the upper troposphere through low-level convergence and subsequent vertical transport of moisture in combination with other processes such as detrainment of cirrus anvils (Betts 1990; Sun and Lindzen 1993).

The strong correlation between deep convection and upper-tropospheric moisture demonstrated above pertains to local variations in FDC and UTH at a scale of roughly (250 km)^2, for example, a 2.5° tropical grid box. However, transport processes play an important role in governing the distribution of upper-tropospheric moisture. Outside the deep convective cluster, the moistening effect of cumulus detrainment and cloud evaporation competes with the drying effect of compensating subsidence. Hence, increased convection may moisten the upper troposphere locally (e.g., over the Tropics); however subsidence and resultant drying of the upper troposphere may take place outside the local area in which the convective disturbance originated (e.g., over the subtropics). Therefore, it is important to examine how the relationship between UTH

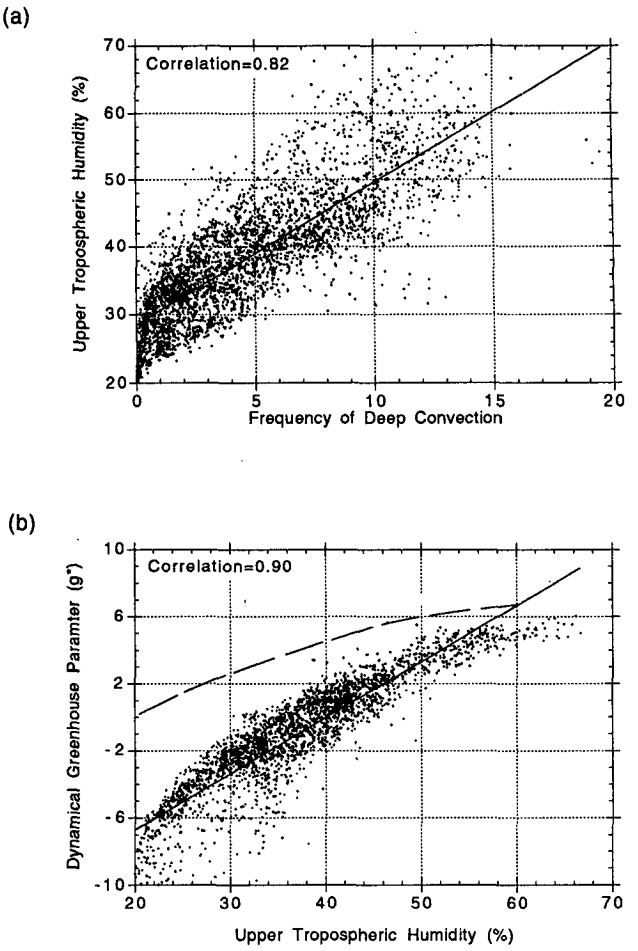

FIG. 3. Scatter plot of the frequency of deep convection versus upper-tropospheric humidity (a) and upper tropospheric humidity versus g^* (b) for all 2.5° grid boxes within the 30°N–30°S tropical belt. The solid line represents a least squares fit. The dashed line depicts a theoretically derived g^* corresponding to the range of observed upper tropospheric relative humidity (see text for details).

behaves at larger spatial scales. Averaging over large domains that encompass regions of both frequent convection and subsidence serves to lessen the possibility that increased moisture in one region is being compensated for by reduced moisture in another. To address this question, the satellite measurements from Fig. 3 are averaged over successively larger domains and scatter plots of spatially averaged FDC versus UTH are constructed (Fig. 4). The results are shown for four domain sizes: (500 km)^2, (1000 km)^2, (2500 km)^2, and (4000 km)^2. Two points are to be made with this analysis: 1) Even at spatial scales of up to ~(4000 km)^2, which is on the order of the meridional length of the (30°N–30°S) tropical belt, the correlation between UTH and FDC is still positive (r = 0.92). We note that even though the number of data points is considerably smaller for the largest spatial domains, the correlations are still significant at the 99% level for

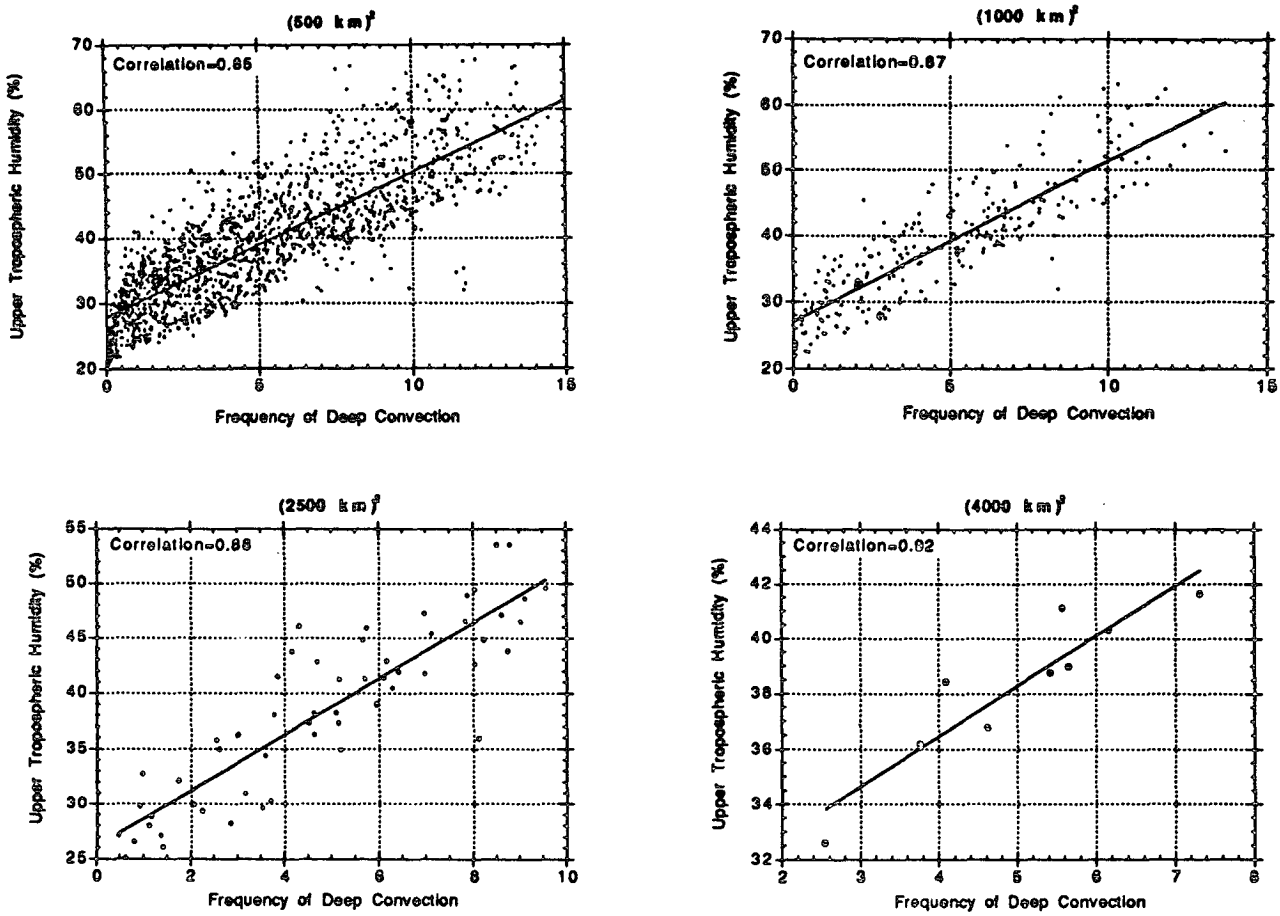

FIG. 4. Scatter plots of the spatially averaged frequency of deep convection versus upper-tropospheric humidity for data within the 30°N–30°S tropical belt. The approximate size of each domain is listed on the title. The solid line represents a least squares fit.

4 degrees of freedom based upon a two-tailed Student's t-test. 2) The relationship between UTH and FDC is insensitive to the size of the averaging domain. Both the correlation and slope vary by less than 20%, while the averaging area varies by nearly two orders of magnitude. Hence, even on very large spatial scales, regions with greater convective activity are associated with increased upper-tropospheric moisture. On both local and regional scales, this analysis demonstrates a positive relationship between deep convection and upper-tropospheric moisture.

b. *Upper-tropospheric humidity and the greenhouse effect*

To understand how changes in convective activity and upper-tropospheric moisture are related to variations in OLR, the regional distribution of g^* is also shown in Fig. 2 (bottom). The values are expressed as a percentage, ranging from −6% to 6%. Values greater than zero indicate a greater than average greenhouse trapping for that SST, suggesting a higher than average water vapor content or a relatively unstable lapse rate. The geographic distribution of g^* displays a strong similarity to that noted for UTH, highlighting the consistency between the two independent datasets. A distinct band of positive g^* coincides with the moist upper-tropospheric regions of the Tropics where convective activity is greatest. The similarity between g^* and UTH is particularly noticeable over the western Pacific warm pool where maxima in both g^* and UTH occur. The anomalously large greenhouse trapping for this region was first noted by Raval and Ramanathan (1989). Hallberg and Inamdar (1993) have referred to this as a "super-greenhouse" effect since the atmospheric greenhouse trapping increases more rapidly with SST than does the surface emission. The observed maxima in UTH over this region is consistent with the work by Hallberg and Inamdar (1993), who used radiative transfer calculations to demonstrate that greater than average relative humidities in the upper troposphere are required to explain the enhanced greenhouse effect for the western Pacific. It also supports the radiosonde observations of Inamdar and Ramanathan

(1994), which suggest the presence of higher relative humidities in the upper troposphere over the western Pacific warm pool. Other prominent features include 1) large areas of negative g^* over much of the subtropics that coincide with weak convective activity and a dry upper troposphere; and 2) zonal bands of positive g^* over the moist, convectively active regions of the midlatitude storm tracks.

To quantify the relationship between upper-tropospheric moisture and the greenhouse parameter, a scatter plot of g^* versus UTH is shown in Fig. 3b. Each data point corresponds to averages over the period February 1984–May 1989 for each 2.5° grid box between 30°N and 30°S. A clear trend of increased greenhouse trapping with increasing upper-tropospheric moisture is apparent. The high correlation ($r = 0.91$) indicates that variations in UTH explain greater than 80% of the regional variations in g^*, confirming the importance of upper-tropospheric moisture on the radiative energy budget. The slope of the observed relationship between UTH and g^* tends to decrease with increasing UTH. This feature reflects the fact that the OLR is more sensitive to variations in UTH in a dry upper troposphere than in a moist upper troposphere (Udelhofen and Hartmann 1994). The combined picture presented by Figs. 3 and 4 is consistent with a positive interrelationship between deep convection, upper-tropospheric moisture, and the OLR. Regions with increased convective activity are associated with greater upper-tropospheric humidity that are, in turn, associated with an increased greenhouse trapping.

Some care must be taken when interpreting Fig. 3b, since other variables that influence the greenhouse trapping (e.g., lapse rate, lower-tropospheric moisture) may be correlated with variations in UTH. To examine the extent to which the observed variations in greenhouse trapping can be attributed to the corresponding observed changes in UTH, the relationship between g^* and UTH determined from satellite data is compared to that predicted from radiative transfer calculations using a random band Malkmus model with a spectral interval of 10 wavenumbers. In performing the calculations, the temperature and lower tropospheric moisture profiles are prescribed using the standard tropical atmosphere (McClatchey et al. 1972), while the relative humidity between 200 and 500 mb is uniformly varied from 20% to 70%. This change in relative humidity approximates the observed range of UTH variation. The OLR resulting from these calculations are then inserted into Eqs. (2) and (3) to determine the corresponding g^*, which is plotted as a dashed line in Fig. 3b. For the prescribed range of UTH, the model calculations reveal a significantly smaller variation in g^* than is observed. Specifically, the model-calculated g^* ranges from roughly 0% (for UTH = 20%) to 7% (for UTH = 70%), whereas the observed range is −7% to 7%, suggesting that increases in UTH are responsible for only about half of the observed increase in dynamical greenhouse trapping. The rest of the increase is likely attributable to variations in lower-tropospheric moisture or lapse rate, which are correlated with the observed variation in upper-tropospheric moisture. This is consistent with radiosonde profiles presented by Inamdar and Ramanathan (1994), which indicated that regions with high upper-tropospheric relative humidities tend to be associated with regions of greater relative humidities in the lower troposphere and larger lapse rates. The range of observed g^* could also be affected by vertical variations in relative humidity within the upper troposphere, and would be larger if the relative humidity lapse rate ($\delta rh/\delta z$) was positively correlated with the vertically averaged relative humidity. No attempt was made to account for such possibilities in performing the radiative transfer calculations.

4. Temporal correlation analysis

a. Deep convection and upper-tropospheric humidity

Figure 5a shows a map of the local correlation between FDC and UTH. The values represent the temporal correlation over the course of the annual cycle calculated from a linear analysis of 48 months of data (February 1985–January 1989) for each 2.5° grid box. Positive (negative) correlations, which are significant at the 99% level assuming 35 degrees of freedom, are denoted by light (dark) shading. The distribution of correlations exhibits a distinctly zonal pattern with a band of significant positive correlations ($r > 0.4$) dominating the Tropics (30°N–30°S) with the highest values occurring over monsoonal regions of southeast Asia, Africa, Brazil, and Central America. Lower correlations ($r < 0.4$) are noted over well-known stratocumulus regions where deep convection rarely occurs. The large area of significant positive correlations evident over most of the Tropics indicates that, on a local scale, months in which deep convection is more frequent are associated with greater moisture in the upper troposphere. This is consistent with the regional analysis, which also demonstrated a positive relationship between deep convection and upper-tropospheric moisture. The question of how the relationship between FDC and UTH behaves at larger spatial scales (e.g., averaged over the entire Tropics) will be addressed shortly. The second interesting feature in Fig. 5a is the distinct difference between tropical and midlatitude correlations. Poleward of 30° latitude, the positive relationship between FDC and UTH breaks down such that UTH becomes uncorrelated with FDC over most of the extratropical storm tracks. Hence, outside the Tropics, variations in convective activity do not exhibit a systematic influence on the UTH. This suggests that (i) the ISCCP-derived FDC may not provide a reliable indicator of convective activity for the midlatitudes, or (ii) other processes in addition to deep convection

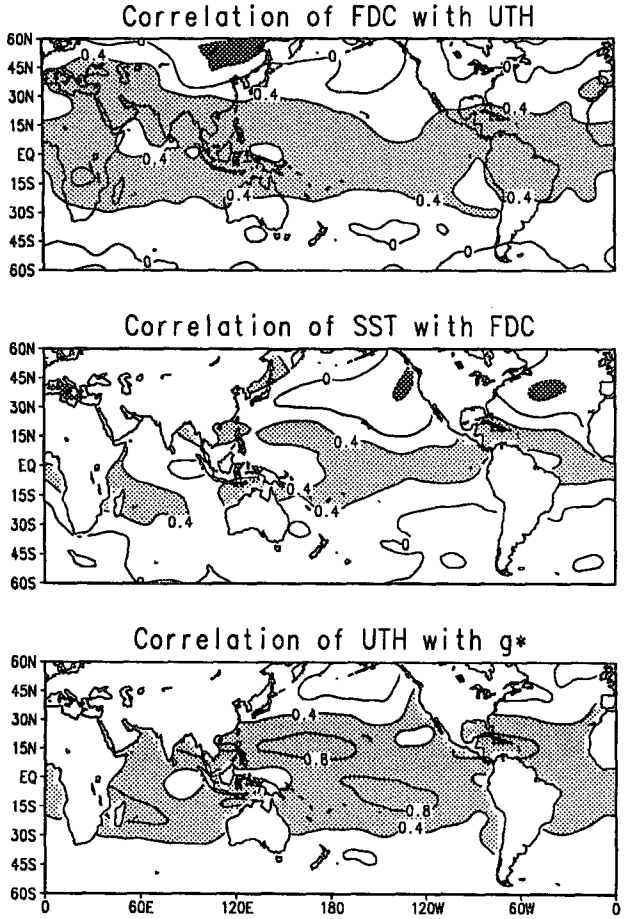

FIG. 5. Local temporal correlation between the frequency of deep convection and upper-tropospheric humidity (a), deep convection and sea surface temperature (b), and upper-tropospheric humidity and g^* (c). The temporal correlations are calculated for each 2.5° grid box from a linear analysis of 48 months of observations. Positive (negative) correlations that are significant at the 99% level are denoted by light (dark) shading. Contour intervals are 0.4.

are important in determining the UTH for this region. For example, large-scale quasi-isentropic transport (Kelly et al. 1991, Pierrehumbert and Yang 1994) and eddy moisture fluxes (Del Genio et al. 1994) have been suggested to be processes in determining the water vapor distribution in the extratropical upper troposphere.

Further information regarding the seasonal behavior of UTH is presented in Fig. 6a, which depicts a map of the ensemble-average difference in UTH for January–July. The largest variations in UTH are observed over the 30°N–30°S tropical belt where seasonal differences frequently exceed 20%. Here, distinct variations in moisture stemming from shifts in the Hadley circulation are apparent. Positive seasonal anomalies form a well-defined band over the Southern Hemisphere equatorial belt with local maxima centered over continental regions and the central Pacific. A similar pattern of negative anomalies occur in the Northern Hemisphere Tropics (30°N–0°), although these anomalies tend to be shifted slightly to the west relative to those in the Southern Hemisphere. These features of the seasonal variation in UTH are broadly consistent with the zonal average change in relative humidity noted by Rind et al. (1991). Over the midlatitudes, seasonal changes in UTH are noticeably smaller, particularly for the Southern Hemisphere. Interestingly, in the Northern Hemisphere land–ocean variations appear to be out of phase with each other. UTH tends to be greater during summer over the midlatitude oceans, whereas it is greater during winter over midlatitude continents. The cause of this land–ocean seasonal asymmetry is not known.

It is worthwhile to compare the seasonal changes in UTH with the corresponding map of seasonal difference in FDC, shown in Fig. 6b. Over the Tropics, the seasonal changes in FDC closely match the patterns of variation in UTH with periods of greater convection exhibiting systematically more moisture in the upper troposphere. However, over the midlatitudes seasonal changes in UTH tend to be nearly out of phase with changes in FDC, particularly for the Northern Hemisphere. For example, Fig. 6 indicates that over the northern Atlantic and eastern North Pacific Oceans UTH increases during the warmer summer (July) while the convective activity actually decreases at this time of the year. This is consistent with the temporal correlation map shown in Fig. 5. Hence, even though the seasonal changes in UTH over the midlatitudes are generally consistent with the changes observed by Rind

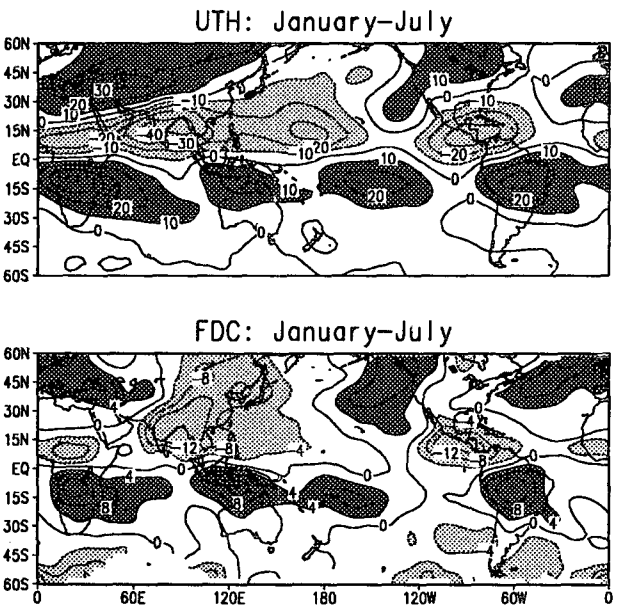

FIG. 6. Geographic map of the seasonal difference (Jan–Jul) in upper-tropospheric humidity (a) and deep convection (b). Positive (negative) differences greater than 10% for UTH and 4% for FDC are denoted by dark (light) shading. Contour intervals are 10% for UTH and 4% for FDC.

et al. (1991), one cannot conclude that they are attributable to local changes in convective activity. Rather, nonlocal processes such as moisture transport from the Tropics may be of greater importance in determining variations in UTH over the midlatitudes and is the subject of future work.

Over the Tropics, seasonal variations in deep convection and upper-tropospheric moisture exhibit coherent patterns of alternating positive and negative anomalies over the entire 30°N–30°S tropical belt (Fig. 6). Variations in one region are often accompanied by compensating variations of the opposite sign in adjacent regions. This is true not only of seasonal variations, but also of interannual variations (see section 5). Thus, although temporal variations in FDC and UTH may be positively related to one another locally, it is not obvious how the these quantities are related when averaged over large spatial domains that encompass regions of both positive and negative anomalies. Along this line, recent studies (Sun and Lindzen 1993; Sun and Oort 1994) have emphasized the importance of understanding the relationship between deep convection and upper-tropospheric moisture when these quantities are averaged over the entire 30°N–30°S tropical belt. Averaging over such large domains serves to remove the uncertainty involving increased moisture in one region being compensated for by reduced moisture in another.

To explore this issue, we spatially average the FDC and UTH measurements over the tropical domain extending globally from 30°N to 30°S. The temporal relationship between the tropical-mean FDC and tropical-mean UTH for the period February 1985–November 1988 is then examined. This particular period was selected because the visible radiances used by ISCCP during this time were calibrated against only one satellite (*NOAA-9*). Consequently, the selection of this time period eliminates the impact of spurious long-term trends in the tropical (or basin) average FDC due to changes in ISCCP visible calibration (Klein and Hartmann 1993). This restriction is not necessary for the local correlation analysis described above because the temporal variations observed locally are much larger than the impact of calibration differences. Additionally, we use 6.7-μm radiances obtained from only the *NOAA-9* satellite to eliminate any effect calibration differences between satellite instruments may have on the tropical average UTH time series. Figure 7 depicts a scatter plot of the tropical-average FDC versus tropical-average UTH. Although there is considerable scatter, the chief feature of this plot is the notable increase in tropical-mean UTH with increasing tropical-mean FDC. The correlation (r = 0.45) is significant at the 98% level assuming every other monthly, tropical-average value is statistically independent. This suggests that even when averaged over both ascending and descending regions of the Hadley circulation, increased convection is associated with an increase in UTH, implying that the net effect of tropical convection is to moisten the upper troposphere.

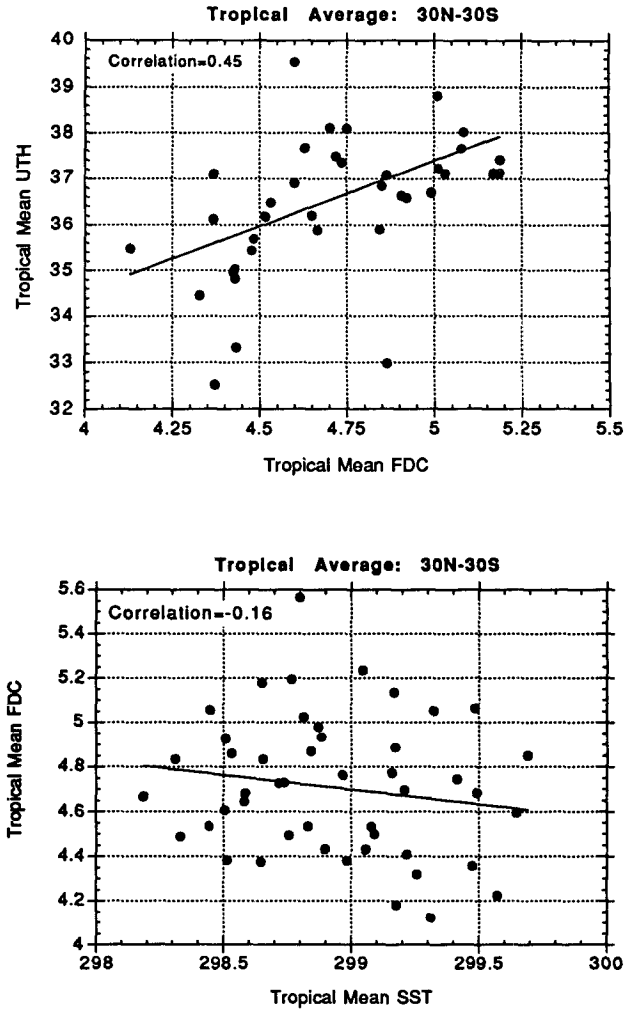

FIG. 7. Scatter plot of the tropical average FDC vs tropical average UTH (a) and tropical average SST vs tropical average FDC (b) for the period February 1985–November 1988. The solid line represents a least squares fit.

b. *Surface temperature and deep convection*

Section 4a noted that the temporal interactions between deep convection and upper-tropospheric humidity exhibit distinct differences between tropical and extratropical regions. The differing behavior of convection between these regions is further demonstrated in Fig. 5b, which depicts a map of the local correlation between monthly mean SST and FDC. A narrow band of significant positive correlations occupies most of the Tropics, indicating that, for these latitudes, warmer SSTs are generally associated with increased convective activity. A notable exception is a narrow band over the equatorial western Pacific and Indonesia where variations in convection tend to be out of phase with

variations in SST. This feature is consistent with the absence of a significant relationship between surface temperature and deep convection in regions of highest SST as noted by Gutzler and Wood (1990). Over the midlatitudes, however, FDC is negatively correlated with SST. The change in correlation reflects a fundamental difference in forcing mechanisms between tropical and midlatitude convection. Over the Tropics, the atmosphere is close to a neutral or conditionally unstable state. Thus, the onset of deep convection requires less dynamic forcing and depends more on the thermal forcing provided by the tropical SST. In the midlatitudes, the atmosphere is closer to a conditionally stable state and initiating deep convection requires a stronger dynamic forcing such as baroclinic instability. Thus, midlatitude convection tends to be greater during winter when baroclinicity is greater even though the SSTs are colder. In addition to the local interactions between FDC and SST, it is also insightful to examine the relationship between these quantities on larger spatial scales. Figure 7b depicts a scatter plot of the tropical-mean SST versus the corresponding tropical-mean FDC. The averaging domains are analogous to those described for Fig. 7a. The most interesting feature of this plot is that temporal variations in the tropical-mean FDC are uncorrelated with changes in the tropical-mean SST. Thus, despite the strong dependence between SST and FDC observed locally, when the data are averaged over large spatial domains, warmer tropical oceans are not necessarily associated with greater convective activity. This feature is consistent with earlier studies, which suggests that warmer SSTs may not necessarily increase deep convection (Betts and Ridgway 1989). Indeed, recent observational (Zhang 1993) and modeling (Knutson and Manabe 1994) studies emphasize the dependence of deep convection to variations in the spatial distribution of SST rather than the magnitude of area-mean SST. For example, Knutson and Manabe (1994) noted that despite an increase in tropical SST by 4–5 K due to a quadrupling of CO_2, the zonal overturning of the atmospheric circulation predicted by the GFDL GCM did not intensify. Thus, as noted by Betts (1990), it is not obvious that a warmer climate resulting from increased CO_2 would necessarily lead to greater convection as is frequently speculated.

c. *Upper-tropospheric humidity and the greenhouse effect*

Figure 5c depicts a map of the temporal correlation between UTH and g^* computed over a 48-month period, February 1985–January 1989. The distribution exhibits two primary features: 1) a band of high positive correlations extending over most of the tropical Hadley belt; and 2) very low correlations over much of the Northern and Southern Hemisphere midlatitude oceans. The significant positive correlations over the Tropics indicate that months with increased UTH are associated with an increase in the atmospheric greenhouse trapping. This result is consistent with the study by Raval et al. (1994) in which temporal variations in clear-sky OLR over the Tropics were shown to be negatively correlated with radiosonde-measured relative humidity. Interestingly, the largest correlations ($r > 0.8$) tend to be offset slightly north or south of the equator, while slightly lower correlations are observed along the equator, particularly in the western Pacific and Indonesia. This band of low correlations coincides with low correlations between FDC and UTH (Fig. 5a), and SST and FDC (Fig. 5b), demonstrating that, within the Tropics, interactions between these variables can have a strong regional dependence. The cause of this anomalous behavior is not clear. The low correlation between UTH and g^* over the midlatitudes indicate that variations in UTH are of less importance in determining the OLR. Other factors, such as variations in temperature (Raval et al. 1994) or lapse rate (Webb et al. 1993), are likely to be more important for these latitudes.

5. Patterns of coupled interannual variability

Previous studies (Lindzen and Nigam 1987; Wallace 1992; Fu et al. 1992, 1994; Hartman and Michelson 1993) have demonstrated that SST affects convection through the large-scale atmospheric circulation and hence the coupling between SST, FDC, and UTH is nonlocal. In this section, singular value decomposition (SVD) is used to identify the dominant modes of coupling between convective activity, upper-tropospheric moisture, and the greenhouse parameter, and to illustrate coherent teleconnection patterns between these variables extending across the Tropics. A thorough description of SVD is presented by Bretherton et al. (1992) and Wallace et al. (1992), therefore only a brief summary of aspects relevant to the present study is provided here. Consider a time series of two data fields, a "left" ($\mathbf{S}$) and "right" ($\mathbf{Z}$), which are normalized to unit standard deviation. Singular value decomposition of the cross-correlation matrix between these fields generates pairs of vectors $\mathbf{p}_k$ and $\mathbf{q}_k$ corresponding to mode k that contain spatial patterns of temporal variation in the left and right fields, respectively. These pairs of patterns represent spatially orthogonal modes of variability and may be ordered such that the first mode ($\mathbf{p}_1$, $\mathbf{q}_1$) explains the most rms temporal covariance between the two fields, the second mode ($\mathbf{p}_2$, $\mathbf{q}_2$) explains second-most, etc. A time series of expansion coefficients a (b) for the left (right) data field are calculated for each mode k by spatially projecting the left (right) data field $\mathbf{S}$ ($\mathbf{Z}$) onto the time series of left (right) pattern vectors $\mathbf{p}_k$ ($\mathbf{q}_k$). The expansion coefficients represent the temporal amplitude and polarity of the particular SVD mode. The magnitude of coupling between the left and right field described by a particular mode is measured by 1) the correlation between the time

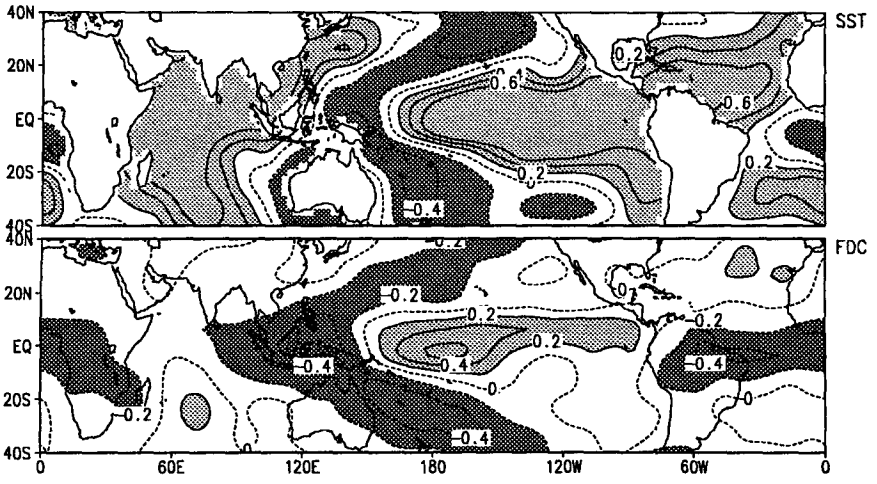

FIG. 8. The heterogeneous correlation pattern of the leading SVD mode of sea surface temperature (top) and frequency of deep convection (bottom); $r = 0.87$, SCF = 30%. Positive (negative) anomalies greater than 0.2 are denoted by light (dark) shading. Contour intervals are 0.2.

series of expansion coefficients for that mode $r[a, b]$ and 2) the squared covariance fraction (SCF), which indicates the percentage of squared covariance between the two fields explained by that particular mode. To illustrate the spatial structure of a particular SVD mode, we construct heterogeneous correlation maps. Defined by Bretherton et al. (1992), these maps display the geographic distribution of the temporal correlation between the right (left) expansion coefficients b (a) and the left (right) data field $\mathbf{S}(\mathbf{Z})$. These fields identify the spatial characteristics in one field that are highly correlated with those in the companion field. To clarify which correlation patterns are being discussed, the heterogeneous correlation between the gridpoint data for the right field $\mathbf{Z}$ and the expansion coefficients a of the left field $\mathbf{S}$ will be denoted as $r[a(\mathbf{S}), \mathbf{Z}]$. Similarly, the heterogeneous correlation between the gridpoint data for the left field $\mathbf{S}$ and the expansion coefficients b of the right field $\mathbf{Z}$ will be denoted as $r[b(\mathbf{Z}), \mathbf{S}]$. As noted by Newman and Sardeshmukh (1995), a similar interpretation of the covariance between two fields can be obtained by correlating the expansion coefficients from a principal component analysis of one field with the time series from the second field.

a. *Surface temperature and deep convection*

First we examine the coupled variability between the SST and FDC fields for the period July 1983–June 1990. The SST and FDC fields are shown first to provide a frame of reference for interpreting variations in the less familiar UTH and g^* fields. The seasonal cycle has been removed from the data so that we may focus on the dominant patterns of interannual variability. Although the pattern of SST variations presented here is very similar to that determined from much longer (40+ year) SST datasets (e.g., Fig. 3b of Lau and Nath 1994), that only 8 years of data are examined suggests that the interannual variations derived here may not necessarily be representative of a longer climatology. For brevity only, the leading mode of variation is presented here; analysis of subsequent modes results in generally similar conclusions regarding the coupled nature of the fields. The heterogeneous correlation patterns for SST $r[b(\text{FDC}), \text{SST}]$ and FDC $r[a(\text{SST}), \text{FDC}]$ are displayed in Fig. 8. The leading mode for the coupled SST/FDC analysis explains 35% of the total squared covariance. The high correlation ($r = 0.95$) between the expansion coefficients indicates a strong temporal coupling between the variations in surface temperature and deep convection. The patterns of SST variations reflect those commonly associated with the El Niño–Southern Oscillation (ENSO). During ENSO events, warm ocean waters in the tropical western Pacific expand eastward into the central/eastern tropical Pacific. A shift in convective activity from the western Pacific warm pool to the central tropical Pacific accompanies this change in SST. These variations in surface temperature and deep convection are revealed in the SVD analysis. The SST variations in the western tropical Pacific are out of phase with those in the central/eastern Pacific, and in phase with those in the subtropical central/eastern Pacific, resulting in a distinct pattern of zonal and meridional anomalies. A similar pattern is evident in the FDC field indicating that, for the tropical Pacific, temporal variations in convective activity associated with ENSO are closely linked to the SST variations. The polarity of the fields is such that regions of increased SST are associated with increased convective activity.

It is evident, however, that coherent patterns of coupled variation between SST and FDC extend well beyond the equatorial Pacific where the ENSO signal is most prominent. Figure 8 indicates that SST anomalies

in the central/eastern Pacific are closely linked with those in the Indian Ocean and tropical North Atlantic Ocean. Indeed, warm events in the central/eastern Pacific are associated with increased SSTs over a broad region of the tropical oceans. Similar large-scale teleconnection patterns are also evident in the FDC field. However, an interesting feature of these patterns is that outside the Pacific, regional anomalies in FDC and SST are no longer in phase with each other. For example, increased convective activity over the central tropical Pacific is associated with reduced convection over much of the remaining tropical belt, particularly the tropical Atlantic and eastern Indian Oceans, despite the fact that these regions are generally associated with positive SST anomalies. Hence, the pattern of interannual variation between FDC and SST seems to behave differently in the Atlantic and Indian Ocean basins as compared to the Pacific Ocean basin. However, since the time period analyzed (1983–90) contains only one full ENSO warm event, the extent to which this result is representative of other ENSO events is questionable.

b. Deep convection and upper-tropospheric humidity

Figure 9displays the heterogenous correlation maps of coupled interactions between FDC and UTH for the period July 1983–June 1990. The SCF for the leading SVD mode is 21% and the correlation coefficient of the expansion coefficients is 0.82. The heterogeneous correlation pattern for FDC $r[b(\text{UTH}),\text{FDC}]$ is nearly identical to the pattern $r[a(\text{SST}),\text{FDC}]$ obtained from the coupled SST/FDC analysis discussed above (Fig. 8). The close similarity between the two correlation maps indicates that the expansion coefficients a(SST) and b(UTH) are very similar, reflecting the fact that interannual variations of SST and UTH are both dominated by ENSO-related forcings.

Comparing Figs. 8 and 9, one can also see that the spatial pattern of interannual change of UTH matches that of FDC more closely than does SST over the Tropics. This suggests that examining the relationship between FDC and UTH can provide more appropriate information for understanding the processes that control upper-tropospheric moisture in Tropics. Because a warm SST does not necessarily increase FDC (Figs. 7 and 8), UTH may not necessarily increase with SST under all conditions. Thus, it is important to understand the relationships both between SST and FDC, and between FDC and UTH to assess the effect of surface temperature on upper-tropospheric moisture in tropical atmosphere.

The heterogeneous correlation pattern for UTH exhibits a clear resemblance to those observed for FDC, demonstrating the influence of ENSO-forced variations in deep convection upon upper-tropospheric moisture. An interesting feature of the anomaly patterns is that outside the Pacific basin the zonal polarity of the patterns reverses. For example, over most of the Pacific (150°E–120°W) the UTH anomalies are positive over the equatorial belt (10°N–10°S) and negative over the subtropical belt (10°–30°N/S). However, over the rest of the Tropics (120°W–150°E) the UTH anomalies are negative over the equatorial belt (10°N–10°S) and positive over the subtropical belt (10°–30°N/S). The phase of the variations are such that areas of positive (negative) FDC anomalies coincide with areas of positive (negative) UTH anomalies, suggesting that even on interannual timescales, regions (or periods) with increased convective activity are closely coupled with increased UTH.

c. Upper-tropospheric humidity and the greenhouse effect

Figure 10 depicts the heterogeneous correlation patterns for the coupled variation of UTH and g^*. The

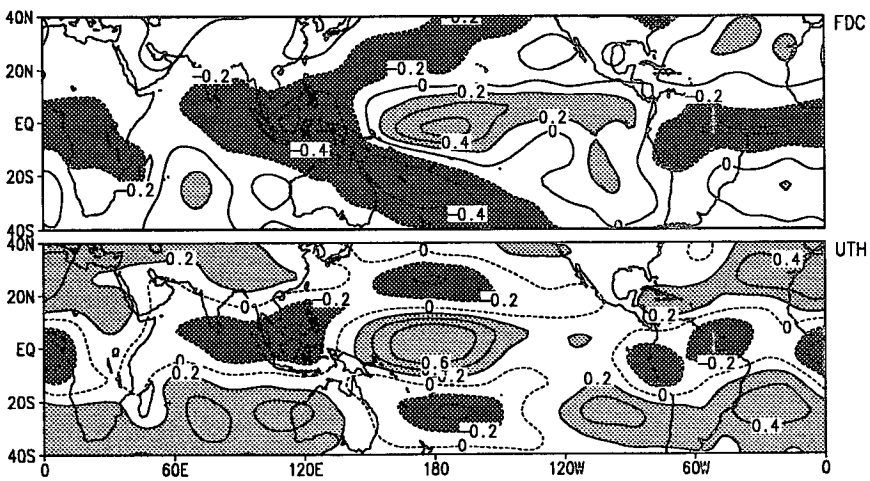

FIG. 9. The heterogeneous correlation pattern of the leading SVD mode of frequency of deep convection (top) and upper tropospheric humidity (bottom); $r = 0.82$, SCF = 21%. Positive (negative) anomalies greater than 0.2 are denoted by light (dark) shading. Contour intervals are 0.2.

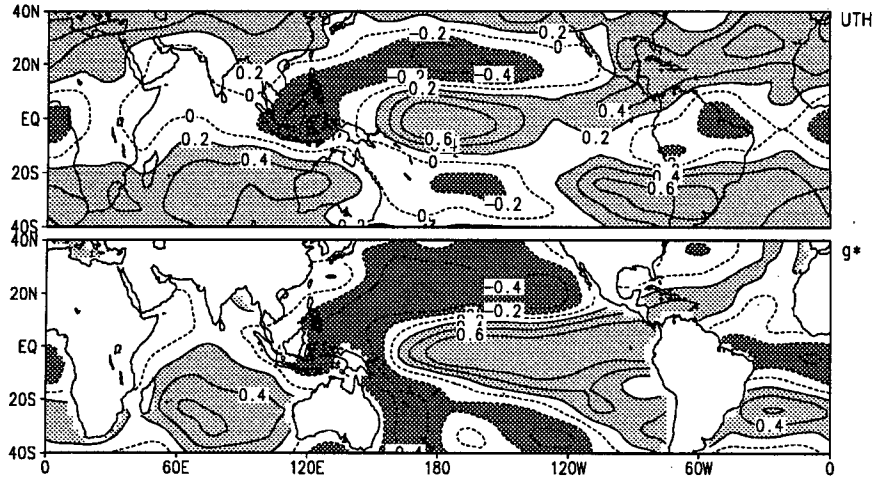

FIG. 10. The heterogeneous correlation pattern of the leading SVD mode of upper-tropospheric humidity (top) and g^* (bottom); $r = 0.95$, SCF = 34%. Positive (negative) anomalies greater than 0.2 are denoted by light (dark) shading. Contour intervals are 0.2.

SCF for the leading mode is 34% and $r = 0.95$. The correlation pattern for UTH closely resembles that derived from the FDC/UTH analysis (Fig. 9), although the correlations are slightly higher suggesting a stronger coupling between UTH and g^* relative to UTH and FDC. Two points are to be made with this figure: 1) Coherent anomalies in g^* extend throughout the 30°N–30°S tropical belt and closely resemble the ENSO pattern described above for UTH. 2) Regions of with positive g^* anomalies generally coincide with regions of positive UTH anomalies indicating that variations in UTH and g^* are in phase with one another. Although it is not possible to separate the relative contribution of changes in lower- and upper-tropospheric humidity to the observed variations in g^*, the analysis does demonstrate that interannual variations in UTH are associated with a similar pattern and polarity of change in greenhouse trapping.

6. Comparison with GCM predictions

The analysis presented so far demonstrates that enhanced convection is strongly correlated with increased upper-tropospheric humidity, which, in turn, is associated with a greater greenhouse trapping. However, these relationships are based upon regional and temporal variations observed within the present climate system, which may or may not serve as suitable surrogates for climate change. Consequently, the extent to which the observed relationships may be extrapolated to describe a climate feedback involving deep convection and upper-tropospheric humidity is uncertain. Rather than making assumptions along this line, a preferred approach is to compare the observed climatic interactions of convection and upper-tropospheric moisture with similar quantities predicted by GCMs. If the GCM-predicted relationships are consistent with those observed, greater confidence can be placed in the model's ability to predict climatic feedbacks involving these interactions. This approach goes beyond simply evaluating model-predicted climatologies of upper-tropospheric moisture (e.g., Soden and Bretherton 1994). Rather, it evaluates the ability of GCMs to predict the observed interactions between certain quantities, thus focusing more directly on the processes that determine the moisture distribution.

In this section, the relationship between convection, upper-tropospheric humidity, and the greenhouse effect predicted by the Geophysical Fluid Dynamics Laboratory (GFDL) GCM are compared with the principal observational results discussed earlier (sections 3–4). The GFDL GCM, described by Wetherald et al. (1991), is a spectral-transform model with 14 vertical levels and is rhomboidally truncated at wavenumber 30, which is approximately equivalent to a horizontal resolution of 2.25° lat × 3.75° long. Deep convection in the model is parameterized via moist convective adjustment (Manabe and Wetherald 1967). The model integration was performed for four years using external conditions prescribed by the Atmospheric Model Intercomparison Project. The predicted UTH fields are computed by inserting the model profiles of temperature and moisture into the TOVS radiative transfer model and simulating the 6.7-μm brightness temperature that would be observed by the satellite under those conditions. For consistency with the observational analysis, the simulated $T_{6.7}$ are then transformed into UTH via Eq. (1) using the same set of regression coefficients ($a = 31.50$, $b = -0.1136$) with p' determined from the model temperature fields. Deep convective activity in the model is determined by recording the frequency (number of time steps per month) at which convective adjustment is performed in the upper troposphere (pressure < 460 mb). This index is then nor-

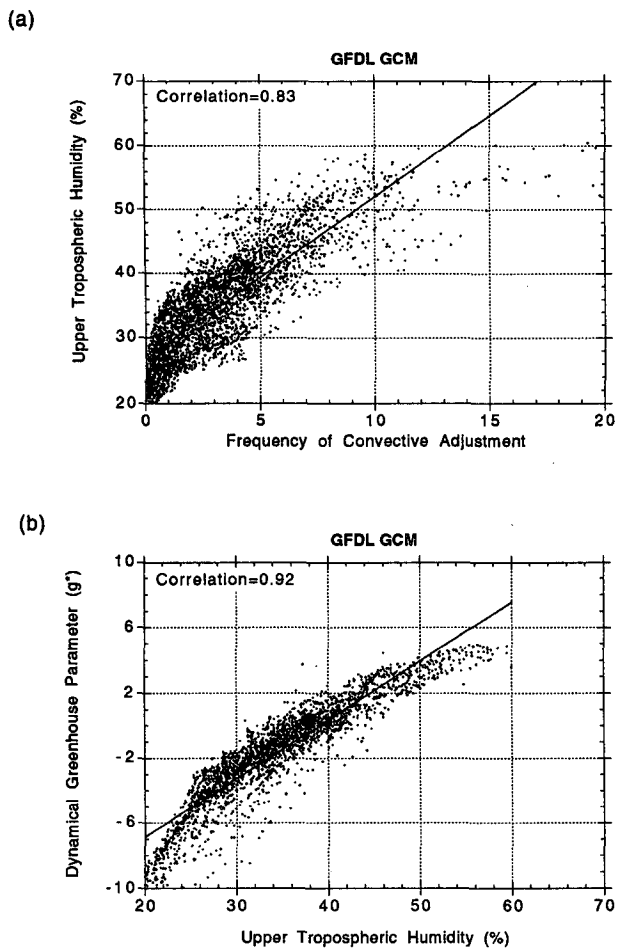

FIG. 11. Scatter plot of the GCM-predicted frequency of moist convective adjustment versus upper-tropospheric humidity (top), and upper-tropospheric humidity versus g^* (bottom) for all GCM grid boxes within the 30°N–30°S tropical belt. The solid line represents a least squares fit.

malized by the number of timesteps within a month to provide a frequency of moist convective adjustment (FCA) index ranging from 0 to 100. Since the FCA index cannot be equated with the satellite measurements of FDC, a quantitative comparison of the observed and modeled indices of deep convection is not feasible. Rather, emphasis here is placed on comparing the qualitative similarity between the observed and predicted relationships of deep convection and UTH.

Figure 11 shows a scatter plot of the model-predicted FCA versus UTH. Each data point corresponds to a 4-year average quantity from each GCM grid box between 30°N and 30°S. The model predictions exhibit a clear increase in UTH with increasing FCA, consistent with the observed relationship between these quantities (compare with Fig. 3). The correlation between regional variations in FCA and UTH is 0.83, which agrees closely with the observed value ($r = 0.82$), indicating that predicted and observed variations in convection explain similar amounts of variance in UTH. The sensitivity of the GCM-predicted relationships to the spatial size of the fields was also examined. The results, listed in Table 1, demonstrate that the model also exhibits little sensitivity to the spatial domain size. Hence, the GCM predictions at both local and regional scales exhibit increased upper-tropospheric moisture in association with increased convective activity, in good agreement with the satellite observations. Figure 11 (bottom) shows a scatter plot of geographic variations between UTH versus g^* from the model. Regions of increased upper-tropospheric moisture in the model are associated with an enhanced greenhouse trapping ($r = 0.93$) in close agreement with the observed relation ($r = 0.91$).

The seasonal variation between deep convection and UTH are also well represented in the model. Figure 12 shows a scatter plot of the seasonal difference (Jan–Jul) of deep convection (ΔFDC) and upper-tropospheric humidity (ΔUTH) from the observations (top) and GCM simulations (bottom) for all grid boxes within the 30°N–30°S tropical belt. On average, both the observations and GCM simulations exhibit greater UTH during the season in which convection is most frequent. The correlation between the observed differences ($r = 0.77$) agrees well with that predicted by the model ($r = 0.75$) indicating that seasonal variations in convective activity explain similar amounts of variation in UTH.

The local temporal correlation between FCA and UTH predicted by the model is displayed in Figure 13a. The value at each grid point represents the linear correlation calculated from a 4-year time series of monthly average quantities. Positive (negative) correlations that are statistically significant at the 99% level assuming 35 degrees of freedom are denoted by light (dark) shading. A band of significant positive correlations dominate most of the Tropics illustrating that months in which tropical convection is more frequent are associated with greater moisture in the upper troposphere. Over the midlatitudes, lower correlations are apparent suggesting that convection is not as important in determining the variations extratropical upper-tropospheric moisture. This pattern of temporal correlation closely resembles that noted for the satellite observations (Fig. 5) and provides further indication of the model's ability to successfully capture the observed temporal variations between deep convection and upper-tropospheric humidity. Figure 13b shows the corresponding map of the temporal correlation between

TABLE 1. Correlation and slope of FDC vs UTH as a function of averaging domain size.

	(250 km)^2	(500 km)^2	(1000 km)^2	(2500 km)^2	(4000 km)^2
Correlation	.83	.84	.89	.92	.94
Slope	2.48	2.57	3.00	3.11	2.85

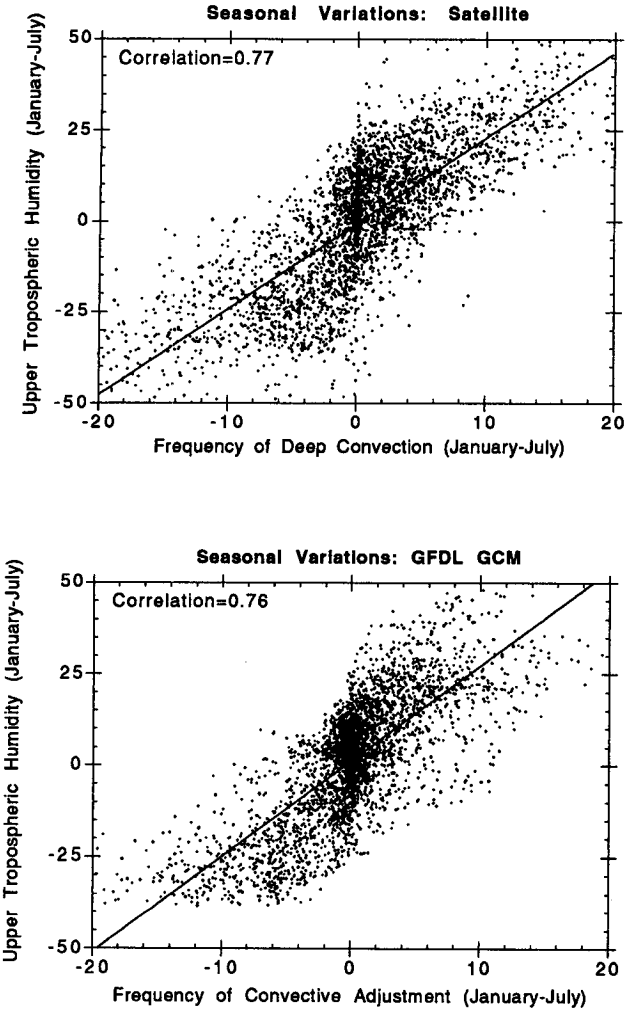

FIG. 12. Scatter plot of the seasonal difference (January–July) of deep convection (ΔFDC) and upper-tropospheric humidity (ΔUTH) from the observations (top) and GCM simulations (bottom). The solid line represents a least squares fit.

monthly average UTH and g^*. The geographic distribution of these correlations displays a large band of positive correlations along the Tropics and lower correlations over the midlatitudes, which is also in good quantitative agreement with the observed distribution (Fig. 5).

Although these comparisons apply only to the present climate, the good agreement of the model-predicted geographic and temporal interactions between deep convection, upper-tropospheric humidity, and the greenhouse effect with those observed provide strong evidence in support of the ability of the GFDL GCM to predict the climatic feedback involving these interactions.

7. Discussion

This study combined satellite measurements from the TOVS 6.7-μm water vapor channel with coincident cloud and radiation budget data from ISCCP and ERBE to analyze the climatological interactions between deep convection, upper-tropospheric humidity, and atmospheric greenhouse trapping. The geographic distribution of deep convection and upper-tropospheric humidity exhibit strikingly similar patterns. Regional variations in FDC are strongly correlated with variations in UTH ($r = 0.82$), indicating that, locally (i.e., at the scale of a 2.5° grid box), increased convection is associated with an increase in upper-tropospheric relative humidity. In addition to examining the local effects, the interaction between convection and upper-tropospheric moisture at large spatial scales was also investigated to reduce impact of moisture transport. It was demonstrated that regional variations between deep convection and upper-tropospheric moisture exhibit little sensitivity to the spatial scale of the analysis. Indeed, even when averaged over spatial domains up to [4,000 km]^2, which encompass areas of both large-scale ascent and descent, the correlation between regional variations in FDC and UTH was still positive and significant at the 99% level. Thus, on both local and regional scales, areas of increased convective activity are associated with increased upper-tropospheric humidity. This evidence supports the contention that the net effect of deep convection is to moisten the upper troposphere. Analysis of ERBE measurements of the outgoing longwave radiation indicate that increased upper-tropospheric humidity is associated with an enhanced greenhouse trapping, demonstrating the im-

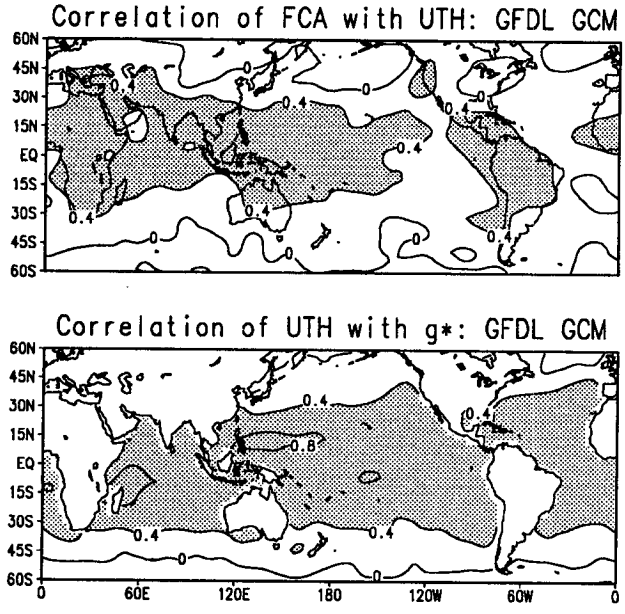

FIG. 13. The GCM-predicted local temporal correlation between FCA and UTH (a) and UTH versus g^* (b). The temporal correlations are calculated for each model grid box from a linear analysis of 48 months of simulations. Positive (negative) correlations that are significant at the 99% level are denoted by light (dark) shading. Contour intervals are 0.4.

portance of moisture transport by deep convection upon the radiative energy balance.

Similar conclusions are obtained from analysis of the temporal interactions between tropical convection and upper-tropospheric humidity. Within the Tropics, local temporal variations in UTH are strongly coupled to variations in FDC. A positive relationship is also observed even when the FDC and UTH measurements are averaged over the entire 30°N–30°S tropical belt, indicating that periods with enhanced tropical-mean convection are associated with increased tropical-mean UTH. Interestingly, although temporal variations in tropical convection and SST are strongly correlated locally, when the observations are averaged over the entire Tropics no significant correlation is observed. This suggests that warmer tropical-mean SSTs are not necessarily associated with an increase in tropical-mean convection. For midlatitude regions, temporal variations in upper-tropospheric humidity exhibit little variability from season to season despite large changes in deep convection. The lack of a clear relationship between deep convection and UTH in the extratropics suggests the importance of other dynamic processes, such as large-scale quasi-isentropic transport, in determining the upper-tropospheric moisture for this region.

Singular value decomposition of coupled interannual variability in deep convection and upper-tropospheric humidity revealed coherent anomaly patterns that extend across the entire Tropics. The pattern of variations reveal substantial changes in zonal and meridional distribution of convection and upper-tropospheric moisture associated with ENSO events and are suggestive of similar changes in the large-scale circulation. Namely, increased convection over the central tropical Pacific is linked zonally with decreased convection over the subtropical central Pacific and meridionally with decreased convection over most of the remaining tropical oceans. The phase of the variations are such that areas of positive (negative) FDC anomalies closely coincide with areas of positive (negative) UTH anomalies. This in-phase relationship, present throughout the Tropics, indicates that even on interannual timescales regions or periods with increased convection are associated with increased UTH. A similar in-phase relationship is observed between anomalies of UTH and atmospheric greenhouse trapping confirming the strong coupling between these fields.

Interestingly, the anomaly patterns for SST and FDC suggest a distinctly different coupling. Within the tropical Pacific, positive SST anomalies are associated with positive anomalies in deep convection; however, outside the Pacific this relationship breaks down. For certain regions, particularly Indonesia and the tropical Atlantic, increased SST locally tends to be associated with reduced convection. An interesting possibility is that the warmer SSTs in the tropical Atlantic and Indian Oceans may actually result from an increase in the absorbed solar radiation at the surface due to a reduction in convective-related cloud cover. In this way, atmospheric circulation anomalies may force SST anomalies rather than vice versa. For example, during ENSO events, local SST anomalies in the tropical Pacific create large-scale atmospheric circulation anomalies that extend well outside the tropical Pacific. These circulation anomalies may, in turn, force SST anomalies in distant regions (i.e., the tropical Atlantic and Indian Oceans) through a change in the solar cloud forcing. A similar "atmospheric bridge" involving interactions between tropical SST and circulation anomalies has been demonstrated in GCM simulations (Lau and Nath 1994).

To evaluate the reliability of GCMs to simulate the interactions between deep convection, upper-tropospheric moisture, and greenhouse trapping, the observed relationships were compared to those predicted by the GFDL GCM. GCM simulations indicate that regions or periods with increased convective activity are associated with increased upper-tropospheric humidity, which are, in turn associated with an enhanced greenhouse trapping. Furthermore, the model predictions of the regional and temporal interactions were shown to be in good agreement with the observed relationships. Thus, despite the model's relatively simplified treatment of moist convective processes, it is successful in simulating the observed climatic interactions between convection, upper-tropospheric moisture, and greenhouse trapping. Although this study can not offer a direct verification of the model's sensitivity under global warming scenarios, the consistency between the modeled and observed relationships within the present climate does support the ability of the GFDL GCM to predict the climatic feedback stemming from externally forced interactions between deep convection and upper-tropospheric water vapor.

Greater understanding of the processes governing the distribution and temporal variation of water vapor, particularly upper-tropospheric water vapor, are of particular importance in answering questions regarding the sensitivity of the earth's climate to increasing greenhouse gases. The global coverage provided by the TOVS 6.7-μm radiances combined with their relatively lengthy archive (dating back to 1979) makes them an ideal source of information for studying upper-tropospheric moisture. Observations from the GOES 6.7-μm channel contain a highly complimentary dataset on upper-tropospheric water vapor by providing both high spatial (16-km field of view at nadir) and temporal resolution (full disk coverage every 30–60 min) measurements. This makes the GOES measurements an ideal source of information for exploring synoptic-scale interactions between convection, upper-tropospheric humidity, and high cloud cover (e.g., Udelhofen and Hartmann 1995). In addition to the 6.7-μm channel, the TOVS archive also contains measurements in the middle- (7.3 μm) and lower- (8.3 μm) tropospheric water vapor channels enabling examination of the wa-

ter vapor distribution within broad layers of the atmosphere. In the past analysis of such large datasets has been hampered by the inaccessibility of the data to interested users; however, the Pathfinder projects for GOES and TOVS, which are designed specifically to make benchmark datasets available, has greatly ameliorated this problem.

Acknowledgments. We would like to thank X. Wu for providing the TOVS data, H. Woolf for providing the CIMSS transmittance model, R. T. Wetherald for assistance with the GFDL GCM, and F. P. Bretherton, A. D. Del Genio, N. C. Lau, V. Ramaswamy, D. Z. Sun, and one of the anonymous reviewers for their constructive comments and suggestions.

REFERENCES

Bates, J. J., and X. Wu, 1995: Interannual variability of upper troposphere water vapor band brightness temperature. *J. Climate,* submitted.

Betts, A. K., 1990: Greenhouse warming and the tropical water budget. *Bull. Amer. Meteor. Soc.,* **71,** 1464–1465.

——, and W. Ridgway, 1989: Climate equilibrium of the atmospheric convective boundary layer over a tropical ocean. *J. Atmos. Sci.,* **46,** 2621–2641.

Bretherton, C. S., C. Smith, and J. M. Wallace, 1992: An intercomparison of methods for finding coupled patterns in climate data. *J. Climate,* **5,** 541–560.

Del Genio, A. D., W. K. Kovari, and M.-S. Yao, 1994: Climatic implications of the seasonal variation of upper troposphere water vapor. *Geophys. Res. Lett.,* **21,** 2701–2704.

Elliott, W. P., and D. J. Gaffen, 1991: On the utility of radiosonde humidity archives for climate studies. *Bull. Amer. Meteor. Soc.,* **72,** 1507–1520.

Fu, R., and W. T. Liu, 1994: Response of tropical clouds to the interannual variation of sea surface temperature. *J. Climate,* submitted.

——, A. D. Del Genio, and W. R. Rossow, 1990: Behavior of deep convective clouds in the tropical Pacific deduced from ISCCP radiances. *J. Climate,* **3,** 1129–1152.

——, ——, W. B. Rossow, and W. T. Liu, 1992: Cirrus-cloud thermostat for tropical sea surface temperature tested using satellite data. *Nature,* **358,** 394–397.

Gutzler, D. S., and T. M. Wood, 1990: Structure of large-scale convective anomalies over tropical oceans. *J. Climate,* **3,** 483–496.

Hallberg, R., and A. K. Inamdar, 1993: Observation of seasonal variations of atmospheric greenhouse trapping and its enhancement at high sea surface temperatures. *J. Climate,* **6,** 920–931.

Hartmann, D. L., and M. L. Michelson, 1993: Large-scale effects on the regulation of tropical sea surface temperature. *J. Climate,* **6,** 2049–2062.

Inamdar, A. K., and V. Ramanathan, 1994: Physics of the greenhouse effect and convection in warm oceans. *J. Climate,* **7,** 715–731.

IPCC, 1990: *Climate Change: The IPCC Scientific Assessment.* Cambridge University Press, 365 pp.

Kelly, K. K., A. F. Tuck, and T. Davies, 1991: Wintertime asymmetry of upper tropospheric water vapor between the northern and southern hemispheres. *Nature,* **353,** 244–247.

Kidwell, 1991: *NOAA Polar Orbiter Data Users Guide.* 281 pp. [Available from the NOAA/NESDIS, Washington, D.C.]

Klein, S. A., and D. L. Hartmann, 1993: Spurious changes in the ISCCP dataset. *Geophys. Res. Lett.,* **6,** 455–458.

Knutson, T., and S. Manabe, 1994: Time-mean response over the tropical Pacific to increased CO_2 in a coupled ocean–atmosphere model. *J. Climate,* **8,** 2181–2199.

Lau, N. C., and M. J. Nath, 1994: A modeling study of the relative roles of tropical and extratropical SST anomalies in the variability of the global atmosphere–ocean system. *J. Climate,* **7,** 1184–1207.

——, and M. W. Crane, 1995: A satellite view of the synoptic-scale organization of cloud properties in midlatitude and tropical circulation systems. *Mon. Wea. Rev.,* **123,** 1984–2006.

Lindzen, R. S., 1990: Some coolness concerning global warming. *Bull. Amer. Meteor. Soc.,* **71,** 288–299.

——, and S. Nigam, 1987: On the role of sea surface temperature gradients in forcing low-level winds and convergence in the tropics. *J. Atmos. Sci.,* **44,** 2418–2436.

Liou, K. N., 1976: On the absorption, reflection and transmission of solar radiation in cloudy atmosphere. *J. Atmos. Sci.,* **33,** 798–805.

Manabe, S., and R. T. Wetherald, 1967: The thermal equilibrium of the atmosphere with a given distribution of relative humidity. *J. Atmos. Sci.,* **24,** 241–259.

McClatchey, R. A., R. W. Fenn, J. E. A. Selby, F. E. Volz, and J. S. Garing, 1972: Optical properties of the atmosphere. Environmental Research Paper AFCRL-72-0497, Air Force Cambridge Research Laboratories, 89 pp.

Newman, M., and P. D. Sardeshmukh, 1995: A caveat concerning singular value decomposition. *J. Climate,* **8,** 352–360.

Oort, A. H., 1983: *Global Atmospheric Circulation Statistics.* National Oceanic and Atmospheric Administration, 180 pp.

Pierrehumbert, R. T., and H. Yang, 1994: Production of dry air by isentropic mixing. *J. Atmos. Sci.,* **51,** 3437–3454.

Raval, A., and V. Ramanathan, 1989: Observational determination of the greenhouse effect. *Nature,* **342,** 758–762.

——, A. H. Oort, and V. Ramaswamy, 1994: Observed dependence of outgoing longwave radiation on sea surface temperature and moisture. *J. Climate,* **7,** 807–821.

Reynolds, R. W., 1988: A real-time global sea surface temperature analysis. *J. Climate,* **1,** 75–86.

Rind, D., E. W. Chiou, W. Chu, J. Larsen, S. Oltmans, J. Lerner, M. P. McCormick, and L. McMaster, 1991: Positive water vapour feedback in climate models confirmed by satellite data. *Nature,* **349,** 500–503.

Rossow, W. B., and R. A. Schiffer, 1991: ISCCP cloud data products. *Bull. Amer. Meteor. Soc.,* **72,** 1117–1133.

Schmetz, J., and O. M. Turpeinen, 1988: Estimation of the upper tropospheric relative humidity field from METEOSAT water vapor image data. *J. Appl. Meteor.,* **27,** 889–899.

Soden, B. J., and F. P. Bretherton, 1993: Upper tropospheric relative humidity from the GOES 6.7 μm channel: Method and climatology for July 1987. *J. Geophys. Res.,* **98,** 16 669–16 688.

——, and ——, 1994: Evaluation of the water vapor distribution simulated in GCMs using satellite observations. *J. Geophys. Res.,* **99,** 1187–1210.

——, and ——, 1995: Interpretation of TOVS water vapor radiances using a random strong line model, *J. Geophys. Res.,* submitted.

——. S. A. Ackerman, D. O'C. Starr, S. H. Melfi, and R. A. Ferrare, 1994: Comparison of upper tropospheric water vapor from GOES, Raman lidar, and CLASS sonde measurements. *J. Geophys. Res.,* **99,** 21 005–21 016.

Stephens, G. L., 1990: On the relationship between water vapor over oceans and sea surface temperature. *J. Climate,* **3,** 634–645.

——, D. A. Randall, I. L. Wittmeyer, D. A. Dazlich, and S. Tjemkes, 1993: The earth's radiation budget and its relation to atmospheric hydrology 3. Comparison of observations over oceans with a GCM. *J. Geophys. Res.,* **99,** 4931–4950.

Sun, D. Z., and R. S. Lindzen, 1993: Distribution of tropical tropospheric water vapor. *J. Atmos. Sci.,* **50,** 1644–1660.

——, and A. H. Oort, 1994: Interannual variations of water vapor in the Tropics. *J. Climate,* submitted.

Udelhofen, P. M., and D. L. Hartmann, 1995: Influence of tropical cloud systems on the relative humidity in the upper troposphere. *J. Geophys. Res.,* in press.

Waliser, D. E., N. E. Graham, and C. Gautier, 1993: Comparison of the highly reflective cloud and outgoing longwave radiation datasets for use in estimating tropical deep convection. *J. Climate,* **6,** 331–353.

Wallace, J. M., C. Smith, and C. S. Bretherton, 1992: Singular value decomposition of wintertime sea surface temperature and 500-mb height anomalies. *J. Climate,* **5,** 561–576.

Wallace, M. J., 1992: Effect of deep convection on the regulation of tropical sea surface temperature. *Nature,* **357,** 230–231.

Webb, M. J., A. Slingo, and G. L. Stephens, 1993: Seasonal variations of the clear-sky greenhouse effect: The role of changes in atmospheric temperatures and humidities. *Climate Dyn.,* **9,** 117–129.

Wetherald, R. T., V. Ramaswamy, and S. Manabe, 1991: A comparative study of the observations of high clouds and simulations by an atmospheric general circulation model. *Climate Dyn.,* **5,** 135–143.

Wu, M. L. C., and L. A. Chang, 1991: Differences in global data sets of atmospheric and surface parameters and their impact on outgoing longwave radiation and surface downward flux calculations. *J. Geophys. Res.,* **96,** 9227–9262.

Wu, X., J. J. Bates, and S. J. S. Khalsa, 1993: A climatology of the water vapor band brightness temperature from NOAA operational satellites. *J. Climate,* **6,** 1282–1300.

Zhang, C., 1993: Large-scale variability of atmospheric deep convection in relation to sea surface temperature in the Tropics. *J. Climate,* **6,** 1898–1913.